

Context-Aware Sensing via Dynamic Programming for Edge-Assisted Wearable Systems

DELARAM AMIRI, University of California, Irvine

ARMAN ANZANPOUR and IMAN AZIMI, University of Turku

MARCO LEVORATO, University of California, Irvine

PASI LILJEBERG, University of Turku

NIKIL DUTT and AMIR M. RAHMANI, University of California, Irvine, USA

Healthcare applications supported by the Internet of Things enable personalized monitoring of a patient in everyday settings. Such applications often consist of battery-powered sensors coupled to smart gateways at the edge layer. Smart gateways offer several local computing and storage services (e.g., data aggregation, compression, local decision making), and also provide an opportunity for implementing local closed-loop optimization of different parameters of the sensor layer, particularly energy consumption. To implement efficient optimization methods, information regarding the context and state of patients need to be considered to find opportunities to adjust energy to demanded accuracy. Edge-assisted optimization can manage energy consumption of the sensor layer but may also adversely affect the quality of sensed data, which could compromise the reliable detection of health deterioration risk factors. In this article, we propose two approaches: *myopic* and Markov decision processes (MDPs)—to consider both energy constraints and risk factor requirements for achieving a twofold goal: energy savings while satisfying accuracy requirements of abnormality detection in a patient’s vital signs. Vital signs, including heart rate, respiration rate, and oxygen saturation, are extracted from a photoplethysmogram signal and errors of extracted features are compared to a ground truth that is modeled as a Gaussian distribution. We control the sensor’s sensing energy to minimize the power consumption while meeting a desired level of satisfactory detection performance. We present experimental results on realistic case studies using a reconfigurable photoplethysmogram sensor in an IoT system, and show that compared to nonadaptive methods, *myopic* reduces an average of 16.9% in sensing energy consumption with the maximum probability of abnormality misdetection on the order of 0.17 in a 24-hour health monitoring system. In addition, over 4 weeks of monitoring, we demonstrate that our MDP policy can extend the battery life on average of more than 2x while fulfilling the same average probability of misdetection compared to the *myopic* method. We illustrate results comparing *myopic*, MDP, and nonadaptive methods to monitor 14 subjects over 1 month.

CCS Concepts: • Theory of computation → Stochastic control and optimization;

Additional Key Words and Phrases: Health monitoring, wearable electronics, Internet of Things, edge/fog computing, edge-assisted control, energy efficiency, context awareness, abnormality detection

This material is based on work supported partially by U.S. National Science Foundation (NSF) WiFiUS grant CNS-1702950 and Academy of Finland grants 311764 and 311765.

Authors’ addresses: D. Amiri and M. Levorato, University of California, Irvine; emails: {damiri, levorato}@uci.edu; A. Anzanpour, I. Azimi, and P. Liljeberg, University of Turku; emails: {armanz, imaazi, pakrli}@utu.fi; N. Dutt and A. M. Rahmani, University of California, Irvine, USA; emails: dutt@ics.uci.edu, a.rahamani@uci.edu.

Permission to make digital or hard copies of all or part of this work for personal or classroom use is granted without fee provided that copies are not made or distributed for profit or commercial advantage and that copies bear this notice and the full citation on the first page. Copyrights for components of this work owned by others than the author(s) must be honored. Abstracting with credit is permitted. To copy otherwise, or republish, to post on servers or to redistribute to lists, requires prior specific permission and/or a fee. Request permissions from permissions@acm.org.

© 2020 Copyright held by the owner/author(s). Publication rights licensed to ACM.

2637-8051/2020/03-ART7 \$15.00

<https://doi.org/10.1145/3351286>

ACM Reference format:

Delaram Amiri, Arman Anzanpour, Iman Azimi, Marco Levorato, Pasi Liljeberg, Nikil Dutt, and Amir M. Rahmani. 2020. Context-Aware Sensing via Dynamic Programming for Edge-Assisted Wearable Systems. *ACM Trans. Comput. Healthcare* 1, 2, Article 7 (March 2020), 25 pages.

<https://doi.org/10.1145/3351286>

1 INTRODUCTION

Interconnected low-cost and miniaturized wearable sensors are increasingly being proposed as an integral part of next-generation health care systems [1–3]. In a recent trend in this class of technological problems, these sensors are integrated within the Internet of Things (IoT) infrastructure to build distributed systems capable of performing highly complex processing of the acquired signals. Of particular interest is the recently proposed edge computing paradigm [4, 5], where compute-capable devices—the edge servers—placed at the edge of the network take over data processing tasks generated by interconnected devices. The low latency of the wireless links connecting the devices to the edge server makes these architectures capable of supporting time-sensitive applications [6, 7].

However, the development of wearable systems for clinical-level continuous monitoring of patients in everyday setting presents critical challenges: (a) the energy supply available to the sensors is severely constrained due to weight and size constraints, and (b) motion artifacts due to body movements diminish the quality of the acquired signals. Problem (b) especially affects sensors measuring vital signs, such as photoplethysmogram (PPG), electrocardiogram (ECG), and electromyogram (EMG) sensors. The signal-to-noise ratio (SNR) of the signals can be improved by increasing the sensing energy. This strategy can further shorten the lifetime of the sensors.

The overarching objective of this work is to mitigate the preceding issues by proposing an edge computing-based architecture supporting a context-aware form of control of the sensors. Specifically, we observe that noise affects the collected signal differently as the monitored subject engages in different activities. For instance, if the person is sleeping, the noise power is much smaller compared to that affecting the same signal acquired when the person is running. Intuitively, knowing the current activity of the person would allow to set a corresponding sensing energy level to reach a desired SNR level.

Intuitively, wearable sensors are not suitable to host such complex reasoning, as detecting the activity would require to process another set of signals, such as from accelerometers. Therefore, we propose to use the edge servers as the central components of a distributed context-aware system: the edge server assisting the sensors will collect their signals, extract the context, (in our case, the activity of the monitored person), and control the sensing parameters using predefined messages. By adapting the sensing energy used by the sensors to the activity, the system can prolong the lifetime of the sensors, thus improving the integrity of the acquired signal over long periods of time, without compromising the quality of the signal.

Based on this general concept and architecture, we fully develop a specific application whose objective is to detect abnormalities in vital signs extracted from PPG sensors [8, 9]. PPG is a low-cost and miniaturized optical sensor widely used in medical and wearable sensors (e.g., fitness trackers, smart rings, smart earrings), which can continuously capture several vital signs such as heart rate, heart rate variability, respiration rate, and blood oxygenation [10]. Based on real-world data, we build a model for normal and abnormal signals, and define corresponding regions in a feature space. In this context, the edge server will detect the current activity of the monitor person and adjust the power used by the PPG sensor to ensure that the misdetection probability is below a predetermined threshold while maximizing the lifetime of the sensor.

To this aim, we develop two distinct strategies. The first strategy is *myopic*, meaning that the sensing power is selected solely based on the current activity. The linear time complexity of *myopic* results in a minimal communication between the edge and sensor layers, as well as a lightweight computation at smart gateways, making

the local control at the edge significantly agile. Conversely, the second strategy builds a statistical model of a person's activities and battery state of charge (SoC) dynamics, which are then used to locate decisions optimal over an extended period of time. Our proposed framework includes the following:

- A hardware prototype of a reconfigurable wireless PPG sensor node
- An edge-based adaptation algorithm for wearable sensors in the context of abnormality detection
- A Gaussian model of the sensing accuracy as a function of activity and input sensor current from real-world measurements to calculate the probability that an abnormal signal is not detected
- Formulation of an optimization problem that enables a trade-off between detection of abnormalities and sensing energy consumption in the sensor.

In summary, work makes the following contributions:

- An edge-based adaptation algorithm for wearable sensors in the context of abnormality detection
- A Gaussian model of the detection accuracy as a function of activity and input sensor current from real-world measurements.
- A myopic strategy optimizing the trade-off between detection of abnormalities and sensing energy consumption.
- A Markov decision process (MDP) solution to track the time-evolving, physical activity of an individual along with the state of the battery.
- Extensive evaluation and results based on a real-world trial involving 20 pregnant women for 7 months (ethically approved human subject trial).

The rest of the article is organized as follows. In Section 2, we provide background on the addressed problem and discuss related work. Section 3 describes the layered architecture of the system. The monitoring and detection frameworks are presented in Section 4. Section 5 discusses the process of extracting vital signs from a PPG signal and setup for collecting activity related data from various subjects. Section 6 presents and discusses numerical results, and Section 7 concludes the article.

2 BACKGROUND AND RELATED WORK

We first introduce state-of-the-art methods in sensor control for energy efficiency (Section 2.1), then we provide background on the PPG sensor used in the proposed study (Section 2.2).

2.1 Related Work

Wearable sensors necessarily are battery-powered devices. Thus, one of the key problems in continuous monitoring of vital signs acquired by these sensors is their limited energy supply. Algorithms to reduce the energy consumption of sensors have been proposed in previous work and widely studied. Recent research has begun to study the energy efficiency of IoT architectures. Scheduling sleeping intervals [11–15], determining duty cycles [16] in the sensor layer, and implementing packet routing [17] are among the methods to deliver energy efficiency to the sensor networks. However, the state of the art lacks the attention toward designing adaptive healthcare IoT architectures capable of controlling system-level parameters based on the context of environment and the state of patients. In 2017, Kaur and Sood [18] presented a solution to determine sleep intervals of sensors based on their residual battery level, usage history, and quality of the measured signal. Additionally in 2017, Tunic and Akar [19] proposed to model as a Markov chain the charging/discharging process of sensors equipped with energy harvesting units. Based on the resulting model, the authors computed the outage probability in a finite time horizon.

Techniques to implement energy efficient networks for biosensors known as the wireless body area network (WBAN) are proposed. Chang et al. [20] proposed a routing protocol for WBAN, considering expected

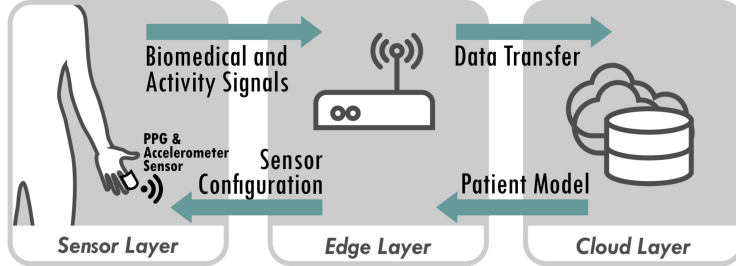


Fig. 1. Three-layer IoT architecture.

transmission count and remaining energy units for optimal path selection. Pradhan et al. [21] compared energy consumption in four protocols—802.15.4, IEEE 802.15.6, SMAC, and TMAC—as hybrid MAC protocols in healthcare.

All of the preceding are exemplars of contributions addressing energy efficiency for IoT sensors. However, none of the authors focused on context-aware models. Herein, we propose a context-aware approach to optimize the energy consumption of the sensors without compromising the probability of detecting anomalous signals.

In 2012–2014, Zois et al. [22–24] proposed MDP-based approaches to detect the activity of a monitored subject by means of imperfect observations acquired by noisy wearable sensors. The framework proposed in those works, which is based on partially observable Markov decision processes, enable exploration of the trade-off between energy consumption, sampling rate, and estimation accuracy. Herein, we use a Markov chain to model the activity, but we use that information to build an optimal detector of anomalies in biosignals. Note that the two approaches could be merged to obtain a holistic activity estimation and anomaly detection.

2.2 Photoplethysmogram

PPG is an optical sensor to measure the amount of oxygenated blood in body tissues. When the heart beats, oxygenated blood penetrates in body tissues through small blood vessels until it delivers all of its oxygen content. The optical characteristics of red blood cells changes according to the amount of oxygen it carries via an internal biomolecule named *hemoglobin*. In PPG, a single wavelength light source illuminates a part of the skin, and a light sensor measures the amount of light reflection or absorption. The sensor output is an oscillating signal, in which each cycle shows the increase and decrease of the oxygenated hemoglobin molecule in blood vessels during individual heartbeats. Although the frequency of the fast-oscillating part of the signal can be used to extract the heart rate, there are also low-frequency oscillations in the signal baseline due to physical changes in the blood vessels surrounding tissues, which reflects the respiration rate. Since the hemoglobin light absorption coefficient differs with different light wavelength, comparing the sensor's output to two different wavelength light sources allows the estimation of blood oxygen saturation (SpO_2).

3 IOT SYSTEM ARCHITECTURE

Herein, we develop a monitoring system based on the emerging three-layer IoT architecture (Figure 1). In healthcare applications, the first layer of this architecture—the one in direct contact with the monitored person—is composed of a body area sensor network capable of capturing biosignals. In our case, this layer consists of a microcontroller, a PPG sensor, an inertial measurement unit (IMU), and a transmission module. The PPG sensor has several power consumption levels (i.e., the LED's current levels) that result in different SNRs as a function of the monitored person's activity. Since our approach finds an optimal solution for the sensor settings by selecting the most efficient power mode, the power levels for this device need to be reconfigurable.

In conventional two-layer IoT architectures, the gateways are simply utilized for networking purposes such as protocol conversion to connect a sensor network to the Internet and cloud infrastructures. Instead, we use

the augmented (smart) version of these gateways [6] and their processing power to implement the core part of the proposed context-aware control: to analyze the incoming data, plan for future configurations of the sensing device, and send the configuration data to the sensor layer. We remark that the three-tier architecture introduces challenges. First, a coherent management of communications and task allocation among the layers necessitates careful design. Then, the distribution of tasks inevitably introduces a delay in the propagation of information throughout the system. Finally, a three-layer design introduces security and privacy concerns. Herein, we establish a fast control loop using the edge server, which is connected to the sensor through a one-hop wireless link. We remark that this strategy grants significant performance gain to the sensor, which has limited computation and energy resources.

As shown in Figure 1, the edge server (e.g., a smart gateway) receives the sensing device information together with the PPG and body acceleration signals and locates the subject’s health status, activity level, and state of the sensing device. It then determines the sensing parameters and sends the new configuration to the sensor node. Note that the overall processing involves some additional steps, such as filtering, encryption, and compression, and sends the preprocessed data to the cloud server, which builds a statistical model of the person’s temporal sequence of activities. The sensing and edge layer are connected through a wireless link, which supports data transfer upstream from the sensors to the edge server and, in the proposed framework, control downstream from the edge server to the sensors.

We use a virtual private server as a cloud server. Similar to an edge device, the cloud server runs an Apache web server on an Ubuntu Linux operating system (OS). A service on the Apache web server is responsible for receiving data from the edge devices and storing them in the OS file system. A MySQL database server stores user information and the index of their related files. These services gradually create a behavior and medical history of the user. We process the stored data through another service to create the weekly Markov model for each user. The server updates the edge device periodically with the latest users’ Markov models.

4 EDGE-ASSISTED ADAPTATION CONTROL

Based on the edge-assisted architecture described in the previous section, the IoT system that we propose uses information related to the context of the monitored subject—the activity in the case study considered here—and the model at the cloud layer to adjust sensing energy. The optimization formulation aims at the minimization of cost measured as energy expense of the sensor node and maximization of the probability an abnormality will be detected. As the first step to formulate the abnormality detection, we model the accuracy of sensor output as a function of the different activities and energy levels.

In Section 4.1, the accuracy model as a function of Gaussian distribution for vital signs is derived. Section 4.2 discusses the stochastic model considering both the activity and the battery model. Section 4.2.1 presents a *myopic* method, which only considers the current patient’s activity to determine the sensing configuration. We build a model for the dynamics of the SoC of the sensor’s battery in Section 4.2.2. In addition, we present an MDP formulation and algorithm that optimizes the current level over a finite horizon based on the activity model stored at the cloud layer.

4.1 Problem Formulation

Based on the biometric PPG signal generated from the pulse oximeter sensor, the gateway calculates vital signs of the monitored person, including heart rate, respiration rate, and SpO₂. We remark that the current level U and the activity X will determine the SNR of the signal used to calculate the features. To evaluate the accuracy of the PPG sensor, we use an ECG sensor as a reference for heart rate, an airflow sensor for respiration, and another PPG sensor with higher signal quality—and therefore energy consumption—as a reference for SpO₂.

Based on the reference signals, we compute the error vectors of the three features: heart rate error $e_1(U, X)$, respiration rate error $e_2(U, X)$, and SpO₂ error $e_3(U, X)$. We calculate the weighted total error vector

$e(U, X) = \{\gamma_1 e_1(U, X) + \gamma_2 e_2(U, X) + \gamma_3 e_3(U, X)\}$. The variables $\gamma_1, \gamma_2, \gamma_3$ are positive weights such that $\gamma_1 + \gamma_2 + \gamma_3 = 1$. We denote as $\rho(e(U, X) | U = u, X = x)$ the probability density function (PDF) of the total error as a function of extracted features during an activity state $X \in \{\text{Sleeping, Sitting, Walking, Jogging, Running}\}$ and current level $U \in \{U_1, U_2, \dots, U_5\}$. For practicality reasons, we assume that the PDF is Gaussian—that is, $\rho(e(U, X) | U = u, X = x) \sim \mathcal{N}(0, \sigma(U, X))$. The variance of error $\sigma(U, X)$ can be derived from the error vector e given current level U and activity state X . The error probability is calculated as the tail probability of the normal distribution. Threshold T corresponds to the maximum total RMSE tolerance in the estimated vital signs. Therefore, the error probability is the following:

$$\mathcal{P}_{\text{error}}(T) = \int_{-\infty}^T \rho_E(e(U, X) | U = u, X = x) de. \quad (1)$$

The formulation derived for error probability can be used to calculate the abnormality misdetection probability. In fact, the abnormality misdetection probability is a function of sensor's error probability (e.g., $P_{\text{error}}(T)$ in Equation (1)) and probability of abnormal vital sign regions. The abnormality misdetection probability formulates the probability that an abnormal event in vital signs is not captured considering the error margin in the sensor's measurements. The error margin in the sensor's measurements can be controlled and adjusted by the threshold T in $P_{\text{error}}(T)$. For instance, a smaller value of T results in accepting smaller values of error probability in the system. Thus, the small values of misdetection probability will require the system to choose higher power levels in the sensor resulting in a higher energy consumption in the sensor.

To formulate the abnormality misdetection probability, we define regions of abnormal vital signs. We assume that the PDF of the vital signs—heart rate, y_1 , respiration rate, y_2 , and SpO₂, y_3 —is Gaussian both in normal and abnormal conditions. We calculate the mean of normal vital signs $\mu_n = \sum_{i=1}^3 \mu_{n,i} \gamma_i$ and variance $\sigma_n^2 = \sum_{i=1}^3 \sigma_{n,i}^2 \gamma_i^2$. Note that these parameters are calculated based on the combined features $y = \gamma_1 y_1 + \gamma_2 y_2 + \gamma_3 y_3$, and we assume that the combined features follow a Gaussian distribution. Abnormal vital signs also follow a Gaussian distribution with mean $\mu_a = \sum_{i=1}^3 \mu_{a,i} \gamma_i$ and variance $\sigma_a^2 = \sum_{i=1}^3 \sigma_{a,i}^2 \gamma_i^2$.

To detect the normal vital signs from abnormal ones, we set the threshold $\tau = \sum_{i=1}^3 \tau_i \gamma_i$ over the thresholds $\{\tau_1, \tau_2, \tau_3\}$ of each individual feature. We then define \mathcal{P}_{DE} as when the abnormality misdetection probability is detecting the abnormal vital signs as normal. A similar formulation considering normal regions of vital signs can be used to model the misdetection of normal vitals as abnormal. In summary, the PDFs of abnormal vital signs (e.g., $f_a(y|U, X)$) and error (e.g., $\rho(e|U, X)$) follow independent Gaussian distributions.

Let $\mathcal{P}_{\text{DE}} = \mathcal{P}(\alpha, \beta, \eta)$ be the abnormality misdetection probability defined as the probability of the following events:

- the sensor's error tolerance $\alpha = \{e(U, X) < T\}$,
- the region of abnormal vital signs $\beta = \{y > \tau\}$, and
- the activity state and current level $\eta = \{U = u, X = x\}$.

Using the chain rule, the joint misdetection probability can be written as

$$\mathcal{P}_{\text{DE}} = \mathcal{P}(\alpha | \beta, \eta) \mathcal{P}(\beta | \eta) \mathcal{P}(\eta). \quad (2)$$

Consider the following upper bound for $\mathcal{P}(\eta)$, with no prior knowledge about U and X ,

$$\mathcal{P}_{\text{DE}} \leq \mathcal{P}(\alpha | \beta, \eta) \mathcal{P}(\beta | \eta). \quad (3)$$

Intuitively, although the distribution of abnormal vital signs is a function of the activity, it is independent with respect to the sensor's current level. Thus,

$$\mathcal{P}_{\text{DE}} \leq \mathcal{P}(\alpha | \eta) \mathcal{P}(\beta | X = x) = \mathcal{P}_{\text{UB}}. \quad (4)$$

Assuming $\mathcal{P}(\alpha | \eta) \sim \mathcal{N}(0, \sigma)$ and $\mathcal{P}(\beta | X = x) \sim \mathcal{N}(\mu_a, \sigma_a)$, we obtain

$$\mathcal{P}_{\text{UB}} = \int_{-\infty}^T \rho_E(\alpha | \eta) d\eta \int_{\tau}^{\infty} f_a(\beta | X = x) dy. \quad (5)$$

By substituting the error probability in Equation (1), we finally obtain

$$\mathcal{P}_{\text{UB}} = \mathcal{P}_{\text{error}}(T) \int_{\tau}^{\infty} f_a(\beta | X = x) dy. \quad (6)$$

We use this form of \mathcal{P}_{UB} along with the energy consumption in the PPG sensor as the main optimization parameters in Sections 4.2.1 and 4.2.2.

4.2 Stochastic Model

The PPG sensor is equipped with a battery of finite capacity. A key part of our model tracks the dynamic of the battery's SoC to enable energy-aware optimization of the used current level. Herein, we consider that Δt is a time slot equal to 15 minutes.

The battery capacity is uniformly quantized to create discrete battery states. Specifically, the SoC in a given time Q_k takes values in $Q = \{Q_1, \dots, Q_K\}$. In the following, we consider the maximum number of battery states K to be 30. The sensing energy consumption is a function of the used sensing current level, which is determined by the control U taking values in the action set $\{U_0, U_1, U_2, \dots, U_5\}$.

We set the states so that the sensor consumes one charge level of the battery in 1 hour if the lowest sensing current level U_1 is used. Thus, the maximum number of hours the sensor can continuously function is equal to 30. The highest current level U_5 consumes five levels of battery charge in an hour. Therefore, the battery will be drained in 6 hours using the highest current level. Action U_0 indicates that the sensor is in sleeping mode, during which the SoC remains the same.

The dynamics of the battery state can be written as

$$Q'_k = \max\{Q_k - E(U), 0\}, \quad (7)$$

where $E(U) \in E = E_1, \dots, E_5$ indicates the number of battery levels consumed at a given time. Denoting the power consumption of the sensor as $C_{\text{TX}}(U)$, Equation (7) can be rewritten as

$$Q'_k = \max\{Q_k - C_{\text{TX}}(U)\Delta t, 0\}. \quad (8)$$

We consider that sensing starts with the maximum full-charged battery at time 0—that is, Q_{30} . Choosing an optimal solution for the current level, the sensor consumes the corresponding energy budget. The discharging probability in the battery depends on the current level chosen as an optimal action. The sensor consumes energy changing the state of battery from Q_k to $Q_{k'}$ where $k' < k$. Therefore, the transition probability during discharging can be defined as

$$q_{k/k'} \triangleq \mathcal{P}(Q'_{k'} | Q_k, U). \quad (9)$$

The sensor is forced to choose a lower current level U during the critical situation when the battery level at a given time is less than the optimal action. For instance, consider that the sensor's optimal current level was chosen to be U_4 but the battery's critical battery level Q_2 does not allow sensing for the next hour. Therefore, the optimal action will be forced to be U_2 to afford the continuation of sensing.

We consider that sensing stops when the battery is drained to the lowest level Q_1 forcing the sensor to choose sleeping action. The user charges the battery only if he or she is not “Walking,” “Jogging,” or “Running,” and the sensor's optimal action would be sleeping mode U_0 . During the charging state, the sensor goes to a sleep mode by choosing the current level to be U_0 . During charging, the state of the battery changes from $Q_{k'}$ to Q_k , where $k' > k$. Therefore, the transition probability during charging will be

$$q_{k/k'} = \mathcal{P}(Q_{k'} | Q_k, U_0). \quad (10)$$

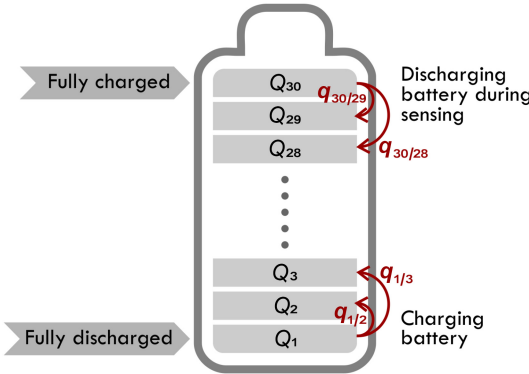


Fig. 2. Markov chain of battery states during charging and discharging modes.

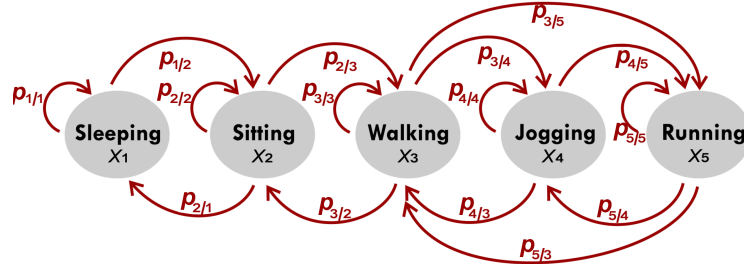


Fig. 3. Markov chain of activities of an individual during one period of 6-hour activity.

Considering the probability of charging and discharging defined previously, the dynamics of the battery during the time can be modeled as a Markov process with states defined with temporal evolution in Figure 2.

The stochastic model considers the activity of the monitored person. In particular, we define a Markov process X whose state space is {Sleeping, Sitting, Walking, Jogging, Running}. Figure 3 shows the connectivity structure of the Markov chain governing the dynamics of X .

Importantly, the statistics of activity dynamics change over time following daily cycles. We capture this characteristic by making the transition probabilities of X . Specifically, we build four different models for daily activities, each corresponding to a 6-hour period. Based on the time of the day, the corresponding Markov chain computed from the history of the activity of the subject will be used to calculate the optimal solution. Assume that each model corresponding to each period of time is denoted by $i \in \{1, 2, 3, 4\}$ during a 24-hour activity. For instance, transition probability from the activity “Sitting” to “Walking” for the first period is denoted as $\mathcal{P}(X_3(1)|X_2(1))$. The transition probability during period i from activity $X_j(i)$ to $X_{j'}(i)$ is defined as

$$p_{j,j'}(i) = \mathcal{P}(X_{j'}(i)|X_j(i)). \quad (11)$$

The Markov model corresponding the i th period of 6 hours per day (e.g., $i \in \{1, 2, 3, 4\}$) will be used to solve the optimization problem. Note that the dynamics of activity change over time, and the model needs to be periodically updated. This becomes particularly apparent in the considered case study, where daily activities are measured in pregnant women. Optimization not only needs to be context aware but also specific to the person and the change over time of the person’s habits. The idea of this model demonstrates the necessity of a self-aware system to adapt its dynamics throughout time. In view of the foregoing, our proposed model in adapting the context-aware system to the activity of the subject results in personalization of the system.

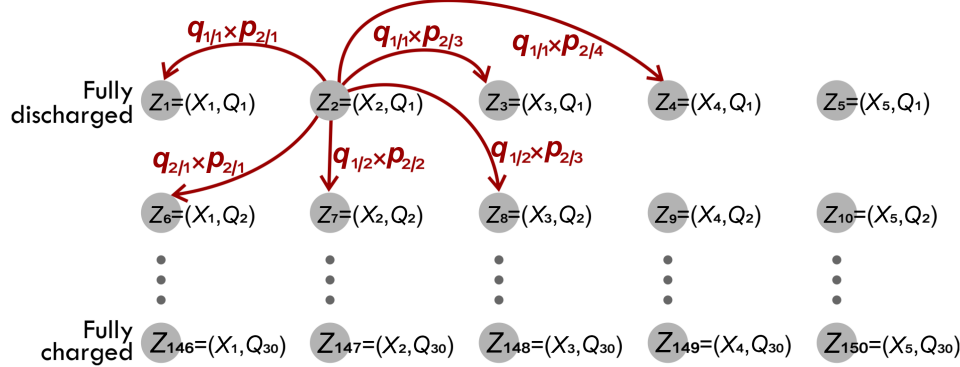


Fig. 4. Markov chain of joint activity and battery state during one period of 6 hours.

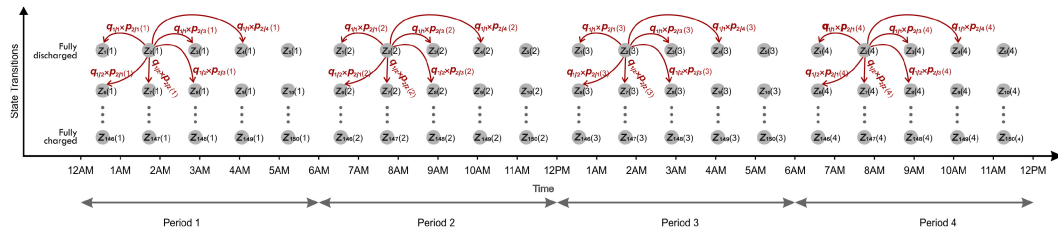


Fig. 5. Markov chain of joint activity and battery states from period 1 to period 4 with 6 hours of duration.

The overall system state Z is defined to be the composition of the battery state Q_k and the patient's activity state $X_j(i)$,

$$Z(i) = (X_j(i), Q_k), \quad (12)$$

with $Z \in \mathcal{Z} = \mathcal{X} \times \mathcal{Q}$. Note that the dynamics of the battery are deterministic and fully defined by the action U and the current SoC Q_k . During the time period i , it is assumed that the transition probabilities between activities are static but then the transition probability will be updated entering the new period. Since the transition probability between activity X and battery level Q is independent, the joint transition probabilities can be written as

$$\begin{aligned} \mathcal{P}(Z'(i)|Z(i), U) &= \mathcal{P}(Q_{k'}|Q_k, U) \times \mathcal{P}(X_j(i)|X_{j'}(i)) \\ \text{or, equivalently,} \\ \mathcal{P}(Z'(i)|Z(i), U) &= p_{j/j'}(i) \times q_{k/k'}(i), \end{aligned} \quad (13)$$

where $\mathcal{P}(Q_{k'}|Q_k, U)$ captures the dynamics of the battery as a function of Q_k , and the chosen action U and $\mathcal{P}(X_j(i)|X_{j'}(i))$ captures the dynamics of activity. We remark that the probability $\mathcal{P}(X_j(i)|X_{j'}(i))$ depends on the time period i . At the end of each time horizon i , a new model of Markov chain with different transition probabilities will be calculated. Therefore, the total transition probability of joint battery and activity states updates in each time slot. In addition, transition probability $\mathcal{P}(Z'(i)|Z(i), U)$ depends on chosen action U . For instance, if the user is "Sitting" and the battery state is fully discharged (e.g., $Z_2 = (X_2, Q_1)$ in Figure 3), the system transitions to the user with "Walking" and battery state Q_2 (denoted as $Z_8 = (X_3, Q_2)$) given the possible action U_0 , with probability $q_{1/2} \times p_{2/3}$. An example of the resulting Markov chain is illustrated in Figure 4. The transition probabilities $\mathcal{P}(X_j(i)|X_{j'}(i))$ are specific to an individual, meaning that the Markov chain is built with the statistics collected over time at the cloud layer. For simplicity, here we assume that the probabilities $\mathcal{P}(X_j(i)|X_{j'}(i))$ are known. Figure 5 demonstrates the dynamics of joint activity and battery states over 24 hours. In this case, the

transition probability between activity states $p_{j/j'}(i)$ is shown as a function of period i . The activity model for the corresponding period i can be used to calculate the total transition probability between joint states. Therefore, dependency of $p_{j/j'}(i)$ on period i results in dependency of total transition probabilities between states on period i as well. This model allows the system to evolve in time based on dynamics of the user's context.

4.2.1 Myopic Strategy. Based on the upper bound for the misdetection probability provided in Equation (6), we define the optimization problem controlling the trade-off between sensing power consumption C_{TX} and probability of misdetection \mathcal{P}_{UB} . The *myopic* optimization problem trades off between sensing power consumption C_{TX} and the probability \mathcal{P}_{UB} in each time slot as follows:

$$\begin{aligned} & \underset{U}{\text{minimize}} \quad C_{\text{TX}}(U) \\ & \text{subject to} \quad \mathcal{P}_{\text{UB}} \leq \theta \\ & \quad \text{or, equivalently,} \\ & \quad \mathcal{P}(\alpha | \eta) \leq \frac{\theta}{\mathcal{P}(\beta | X = x)} = \zeta. \end{aligned} \tag{14}$$

We define the Lagrangian multiplier λ to solve the equivalent optimization problem:

$$\mathcal{L}(U, \lambda) = C_{\text{TX}}(U) + \lambda(\mathcal{P}(\alpha | \eta) - \zeta). \tag{15}$$

Taking the derivative with respect to the sensor's current level,

$$\frac{\partial C_{\text{TX}}(U)}{\partial U} + \lambda \frac{\partial \mathcal{P}(\alpha | \eta)}{\partial U} = 0. \tag{16}$$

We obtain a linear relation between power consumption and current level:

$$a_U + \lambda \frac{\partial \mathcal{P}(\alpha | \eta)}{\partial \alpha} \frac{\partial \alpha}{\partial U} = 0. \tag{17}$$

Given the Gaussian PDF of α and linearity between α and U , we have

$$a_U + \lambda b_U \sum_{i=1}^N \mathbb{1}[U = U_i] \frac{\partial \Phi_i(\alpha)}{\partial \alpha} = 0. \tag{18}$$

The optimal (U^*, λ^*) can be then calculated as

$$\sum_{i=1}^N \mathbb{1}[U = U^*] \frac{\partial \Phi_i(\alpha)}{\partial \alpha} = -\frac{a_U}{\lambda^* b_U}. \tag{19}$$

Using this formulation, we developed Algorithm 1 to determine the optimal current level in each slot. If the number of possible current levels is equal to N , the complexity of this search is $O(N)$.

4.2.2 Optimization over a Finite Horizon. The *myopic* method solves the optimization problem with linear time complexity. In this section, we propose the second method to optimize in a longer perspective. In our prototype system, the edge layer keeps track of patient's activity state along with the battery state of the PPG sensor. The cost function in this method is defined as a function of the power consumption and the upper bound for misdetection probability (e.g., Equation (6)). The twofold goal is to minimize the cost while tracking the system and patients' states. To this end, we must propose a method that determines the sensor's current level to minimize the accumulative cost over a finite time horizon.

Optimal strategy. The Markov process defined earlier in Section 4.2 allows the computation of strategies optimizing the current level over a temporal horizon, which is moved in a sliding window fashion. Optimality is defined over a cost jointly capturing sensing power consumption and misdetection probability in the upper-bound form provided in the previous section. In fact, misdetection probability \mathcal{P}_{UB} as a function of activity state

ALGORITHM 1: *Myopic* method to control the sensor's current

```

1: procedure SOLUTION( $\tau, T$ ) ▷  $\tau$  and  $T$  are thresholds at a given time  $t$ 
2:   Extract activity level  $X$ 
3:   for  $U \in \{U_1, \dots, U_5\}$  do
4:     Calculate the variance of the error  $e(U, X)$ .
5:     Calculate tail Gaussian  $\mathcal{P}(e | U = u, X = x)$ 
6:     Estimate  $\mathcal{P}_{DE}$  using  $\mathcal{P}_{UB}$ .
7:     if  $\mathcal{P}_{UB} < \tau$  then return  $u$ 
8:     else
9:       continue
10:  until the system is terminated

```

X and current level U directly influence the total cost. Therefore, the total cost $C(Z, U)$ can be written as a function of joint state Z and current level U :

$$C(Z, U) = \omega \mathcal{P}_{UB}(U, X) + (1 - \omega) C_{TX}(U). \quad (20)$$

Given an initial state $X(0) \in X$ and $Q(0) \in Q$, and the finite horizon \mathcal{T} , we calculate an average expected reward under the action U :

$$\mathcal{J}(Z, U) = \frac{1}{\mathcal{T}} \left[\sum_{t=0}^{\mathcal{T}-1} \gamma^t C(Z, U) | Z(0) \right], \quad (21)$$

where we find the expected function under action $\mathcal{U} : \mathcal{Z}' \rightarrow \mathcal{Z}$. Note that discount factor $0 \geq \gamma < 1$ is typically chosen close to 1.

Optimal action. The goal is to minimize \mathcal{J} over a finite time horizon with a given initial state $Z(0)$ that achieves the minimum cost:

$$U^* = \underset{U}{\operatorname{argmin}} \mathcal{J}(Z, U). \quad (22)$$

Using this optimization formulation, we developed Algorithm 2 to determine the optimal current level in a given time. In other words, the edge processor determines the current level such that the total cost as a function of misdetection probability and the sensor's power consumption will be minimized.

5 SETUP AND DATA

In this section, we first describe in detail the system setup in Section 5.1, and in Section 5.2, we describe the clinical trial at the base of this study and its output data.

5.1 Setup

We now provide some specifics of the IoT system we developed. The sensing device, besides the actual PPG sensor, is equipped with a microcontroller to read data from the sensor, a Flash memory to store data temporarily, and a wireless data transmission module to send the recorded data. We use the ESP8266-12E board, which integrates all mentioned components in a single board. In the specific board we used, a full TCP/IP stack is integrated with an L106 32-bit RISC microprocessor core running at 80 MHz, with 96 KB of on-chip SRAM and 4 MB of external Flash memory. For the sensor, we use a MAX-REFDES117 PPG sensor board, which is highly configurable and provides a digitized signal through I2C communication. We program the microprocessor using the C programming language to configure the sensor board internal registers. The sensing device connects to the edge device via a WiFi connection. It has a permanent configuration memory that records the user information and credentials of three different WiFi networks. At the beginning of the operation, the sensor node connects

Table 1. System States with Sensing Power Consumption

State	Power Consumption
Recording mode: LED setting: 0.8 mA	69.30 mW
Recording mode: LED setting: 3.5 mA	73.26 mW
Recording mode: LED setting: 6.2 mA	79.86 mW
Recording mode: LED setting: 9.3 mA	84.15 mW
Recording mode: LED setting: 12 mA	89.43 mW

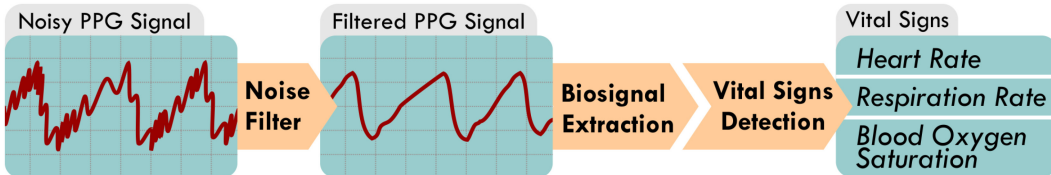


Fig. 6. Local data analysis to extract vital signs from raw PPG signals.

ALGORITHM 2: MDP method to control the sensor's current

```

1: procedure SOLUTION( $\tau, T$ )
2:   Extract activity level  $X$ 
3:   Estimate battery level  $Q$ 
4:   Calculate the variance of the error  $e(U, X)$ .
5:   Calculate tail Gaussian  $\mathcal{P}(e \mid U = u, X = x)$ 
6:   Estimate  $\mathcal{P}_{DE}$  using  $\mathcal{P}_{UB}$ .
7:   Find the transition matrix  $\mathcal{P}_{z'z}(U)$  based on time  $t$  on the portion of the day
8:   for state  $Z \in \{Z_1, \dots, Z_{150}\}$  do
9:     for state  $U \in \{U_0, \dots, U_5\}$  do
10:      Use Equation (20) to compute cost  $C(Z, U)$  for transition matrix  $\mathcal{P}_{z'z}(u)$ 
11:      Use Equation (22) to find optimal action  $U^*$ 
12:   until the system is terminated
  
```

to a WiFi network and asks the edge device to send initial configuration instructions, which include the PPG LED power, recording duration, and hibernate state duration. Next, the sensing device begins to record the PPG signal on the Flash memory and then goes to the hibernation mode for the duration defined in the configuration instructions. After the hibernation period, it connects again to the edge device via the WiFi connection, sends the recorded data, waits for the edge device to process the transferred data, receives the results as a new set of configuration instructions, and initiates a new recording cycle. Note that the sensor turns the radio communication circuitry off during the recording and hibernation to save energy. Table 1 summarizes the system's power consumption specifications.

The edge device is a Linux-based computer running an Apache web server. It receives each set of the recorded data from the sensing device via several HTTP Upload POST requests, merges data chunks into one file, analyzes the data, and returns the new configuration in reply to the latest HTTP request. As shown in Figure 6, local data analysis on the edge device consists of two sequential phases: biosignal extraction and vital signs detection.

Biosignal extraction. Respiratory and heartbeat signals are extracted from the raw PPG signal. Different studies proposed various techniques that can be categorized into two major classes: feature-based extraction and filter-based extraction [25, 26]. The former class first derives features from the waveform to extract respiratory and heartbeat signals [27]. These methods might be, nevertheless, inappropriate in real-world applications since the

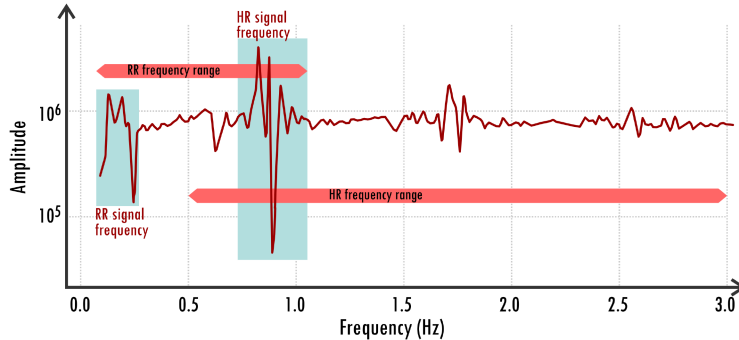


Fig. 7. PSD of a 1-minute PPG signal while the user is sleeping. HR, heart rate; RR, respiration rate.

feature quality is highly susceptible to motion and ambient noise. Such artifacts are inevitable in wearable devices as patients engage in different activities in nonclinical settings. However, filter-based extraction techniques remove the artifacts before deriving the biosignals, filtering the raw PPG signal [28].

We adopt a filter-based technique by designing two band-pass filters for heartbeat and respiratory signal extraction. In general, the biosignals have different frequency ranges: 0.1 to 1 Hz (6 to 60 breaths/minute) and 0.5 to 3.3 Hz (30 to 180 heartbeats/minute). The boundaries could be selected as the filters' cutoff frequency. However, such a naive approach leads to high error rates, as the pass range is too broad. Then, we select the cutoff frequency using the peak values in the power spectral density (PSD) of the PPG signals [29]. Figure 7 shows the PSD as a function of frequency for a 1-minute PPG signal while the user is sleeping.

The peak in the heart rate frequency range reflects the heartbeat signal frequency. Similarly, the respiratory signal frequency is selected using the peak in the respiration rate frequency range. As the respiration rate frequency range might contain the heart rate frequency peak, we first extract the heartbeat signal and remove the heart rate peaks, and then we acquire the respiratory signal. The filter's cutoff frequencies are dynamically selected during the monitoring with respect to the incoming signals. Note that an acceptable SNR is necessary, as an excessive distortion of the signal would impair the process.

Vital signs detection. Several time-domain and frequency-domain techniques can be exploited to derive the respiration rate and heart rate from the biosignals [25]. In our setup, we use a peak detection algorithm where the peaks are obtained by detecting local maximum points in the derivative of the biosignals. The period between two consecutive peaks reflects the respiration rate and heart rate values.

In contrast to the respiration rate and heart rate, the SpO₂ is calculated using a feature-based technique. As indicated in Figure 8, four features—AC_{RED}, DC_{RED}, DC_{IR}, and AC_{IR}—are acquired from the infra-red (IR) and red signals. Such features are obtained by mapping consecutive local extrema of the heartbeat signals into the raw PPG signals. The SpO₂ is calculated using the following equation:

$$R = \frac{AC_{RED} \cdot DC_{IR}}{AC_{IR} \cdot DC_{RED}}, \quad (23)$$

$$SpO_2 = \alpha R^2 + \beta R + \gamma, \quad (24)$$

where α , β , and γ are constants determined by the sensor's specification [30].

5.2 Data Collection

To evaluate the accuracy model of the PPG sensor's measurements, we first collect data for the PPG signal during different activities. We conduct our 5-hour experiment with 25 different combinations, in which a healthy subject is monitored during "Sleeping," "Sitting," "Walking," "Jogging," and "Running" and the sensor's current level is

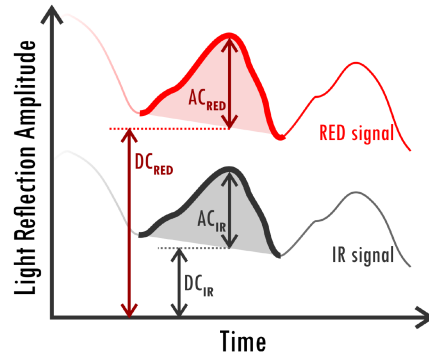


Fig. 8. Features in the PPG signals for SpO_2 calculation.

varied with different values (e.g., 0.8 mA, 3.5 mA, 6.3 mA, 9.2 mA, and 12 mA). Each experiment lasted for 12 minutes. Windows of 30 seconds were used to calculate the vital signs from the PPG signal. The PPG signal from the sensor is preprocessed and filtered, and the features SpO_2 , heart rate, and respiration rate are evaluated for each combination of current level and activity.

Simultaneously, we use three different reference sensors to compare the calculated vital signs from our proposed PPG sensor with a ground truth. We use a chest strap ECG sensor to capture the reference heart rate, an airflow sensor for a respiration reference, and another PPG sensor with higher signal quality as a reference for SpO_2 . We then calculated the error between calculated vital signs and the reference signal to model the accuracy of measurements.

To model and test our proposed algorithms, physical data is recorded. The physical activity data is part of a longitudinal study conducted to investigate the maternal body changes on pregnant women for 7 months (i.e., 6 months of pregnancy and 1 month postpartum). The study was performed in collaboration with the Department of Nursing Science, University of Turku (UTU) and Turku University Hospital, and in accordance with the code of ethics of the World Medical Association (Declaration of Helsinki). In addition, it was approved by the joint ethics committee of the hospital district of Southwest Finland (35/1801/2016) and Turku University Hospital.

Between May 2016 and June 2017, 20 pregnant women were selected and recruited in Southern Finland, considering different criteria such as “singleton pregnancy,” “18 as the lower age limit,” and “gestational age less than 15 weeks.” Data collection was performed 24/7 via a lightweight fitness tracker (i.e., Garmin Vivosmart HR) [31] consisting of a PPG sensor and IMU. The data were regularly transferred to remote computers for storage and postprocessing. The physical activity data utilized in this work was abstracted from the user’s steps and hand movements in every 15-minute interval [32, 33]. Data from six subjects were rejected due to discontinuity in data recording, with more than 50% of missing data. The output of the study allowed us to build the transition probabilities capturing the dynamics of the activity engaged by the monitored person. Note that the model evolves over time and is specific to a person. Therefore, the cloud layer continuously updates the model and periodically sends it to the edge server.

6 NUMERICAL RESULTS

In this section, we provide extensive results assessing the performance of the proposed system and optimization framework. To assess the accuracy, the features extracted through the PPG sensor are compared to a ground truth. We first calculate the total variance of $RMSE$ to determine errors in the sensor with different activities and different current levels of the PPG sensor. Figure 9 shows that the variance decreases when the current level is increased. The variance increases in strenuous activities, such as “Jogging” or “Running,” due to noise caused by motion artifacts. Using the total variance of $RMSE$, we model the probability of misdetection in abnormality

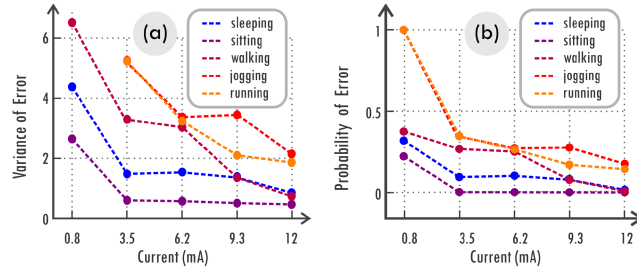


Fig. 9. (a) Total error variance for activity X and current level U . (b) Error probability for activity X and current level U with maximum $RMSE = 2$.

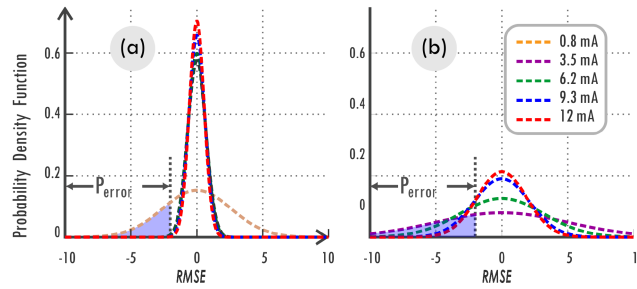


Fig. 10. Error probability when $RMSE = 2$ for different current levels during two states: sitting (a) and running (b).

to follow a Gaussian distribution. The PDF of two activities is shown in Figure 10. Higher values of variance in lower current levels resulted in higher values of probability of error (e.g., $\mathcal{P}_{\text{error}}$ in Equation (1)). Figure 10 shows the PDF of “Sitting” and “Running” with the calculated error variance. Higher values of variance in lower current levels lead to higher values of the error probability $\mathcal{P}_{\text{error}}$. The shaded regions in Figure 10(a) and (b) correspond to $\mathcal{P}_{\text{error}}$ with a threshold of $RMSE, T = 2$. A decrease in probability of error with a higher current level during vigorous decreases is more evident. In addition, $\mathcal{P}_{\text{error}}$ is 1 during “Running” or “Jogging” with the minimum current level of 0.8 mA. Thus, the heart rate, respiration rate, or SpO_2 cannot be extracted from the acquired signal due to the vigorous movements of the subject. The lowest acceptable current level for activities such as “Running” and “Jogging” is 3.5 mA.

Myopic strategy. First, We evaluate the *myopic* strategy presented in Section 4.2.1. We first monitor a healthy individual for 24 hours. A 3D acceleration signal is used to continuously estimate the user’s physical activity. The accelerometer sensor is placed at the user’s hand, and hand movements are tracked to extract the user’s steps. The acceleration signal is filtered, mitigating ambient noise, and steps are counted in each time interval. Moreover, when the user is still (i.e., no step is detected), the orientation of the user is leveraged to differentiate between sitting and sleeping.

First, we set $T = 2$ to be the predefined threshold of the $RMSE$. We then calculate the error probability for all possible power levels. The *myopic* algorithm chooses the lowest power level that satisfies the maximum misdetection probability \mathcal{P}_{UB} calculated in Equation (14). Vigorous activities necessitate accurate monitoring, which leads to choosing higher power levels. In contrast, lower power levels can satisfy the same constraint on the probability of error in activities such as sleeping or sitting. In the results, we set the maximum probability of error to $\zeta = 0.17$ and set the weights as $\gamma_1 = 0.25, \gamma_2 = 0.35, \gamma_3 = 0.4$. Using these weights, we determine the mean and variance of abnormal vital signs for each activity. In the considered case and chosen parameters, the aggregate of normal vital signs y follows the distribution $\mathcal{N}(\mu_n, \sigma_n)$ with $\mu_n = \{57.72, 60.43, 74.29, 83.97, 91.53\}$ and $\sigma_n = \{0.25, 0.73, 1.17, 1.45, 0.62\}$ in the order of “Sleeping,” “Sitting,”

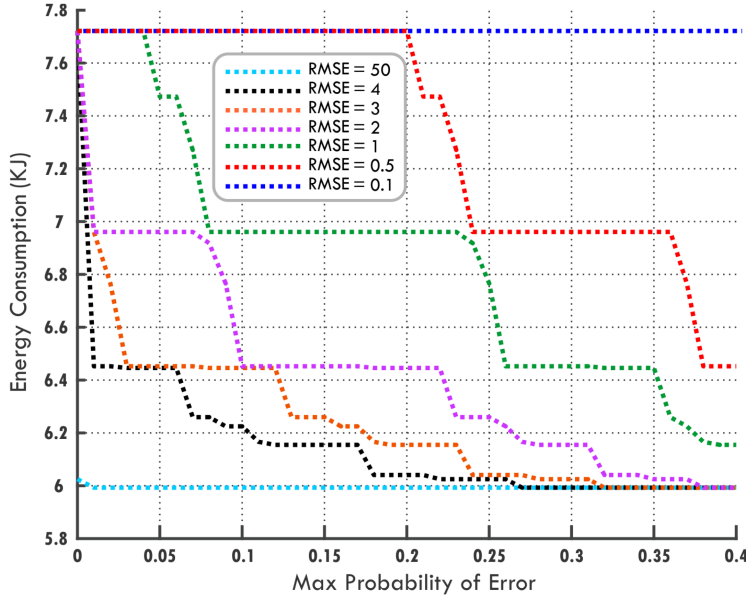


Fig. 11. Sensing energy consumption as a function of maximum probability of error with different RMSE levels.

“Walking,” “Jogging,” and “Running,” respectively. Abnormal vital signs follow the distribution $\mathcal{N}(\mu_a, \sigma_a)$, where we set $\mu_a = \{56.83, 61.07, 74.15, 81.50, 97.00\}$ and $\sigma_a = \{2.02, 0.71, 2.29, 1.67, 2.88\}$, respectively, and each element of the vectors corresponds to a different activity as indicated earlier. The threshold τ defined in Equation (5) is the intersection of two Gaussian distributions corresponding to normal and abnormal vital signs. The cumulative distribution function (CDF) for abnormal vital signs is calculated with $\tau = \{57.20, 60.73, 72.76, 82.68, 89.58\}$.

Based on these parameters, the probability $\mathcal{P}(\beta | X = x) = \{0.57, 0.68, 0.72, 0.76, 0.99\}$ is then derived according to Equation (5). Assuming the predefined threshold $\zeta = 0.17$ in error probability of the sensor and $\mathcal{P}(\beta | X = x)$, the new threshold is set for the probability of misdetection to fulfill the upper bound $\theta = \zeta \times \mathcal{P}(\beta | X = x)$ (see Equation (14)). The threshold $\theta = \{0.09, 0.11, 0.12, 0.13, 0.17\}$ is the final vector corresponding to the desired upper bound of misdetection probability \mathcal{P}_{UB} in the order of “Sleeping,” “Sitting,” “Walking,” “Jogging,” and “Running,” respectively.

We first evaluate the *myopic* method to monitor a subject for 24 hours. We monitor the subject’s activity and compare constant power consumption with the *myopic* method. During the 24-hour experiment, we measured 5,983.4 J and 7,721.4 J consumed by the lowest and highest sensing power, respectively. The *myopic* strategy achieved an energy consumption to 6,417.5 J, with an average sensing power consumption of 74.32 mW, equivalent to a 16.9% reduction compared to the 89.43 mW of the highest sensing power level. Although using the lowest current level results in a lower overall energy consumed by the sensor, using this setting leads to an unacceptable $\mathcal{P}_{error} = 1$ during “Jogging” and “Running.”

Figure 11 illustrates the trade-off between the constraint on the maximum error probability and overall energy consumption in a 24-hour temporal period. The *myopic* algorithm can detect abnormalities with maximum tolerance threshold of RMSE = 50 by choosing the lowest current level. This setting leads to an energy expense equal to 5,983.4 J. Setting the maximum error tolerance to RMSE = 0.1 or less results in choosing the highest current level with the lowest probability of error inevitably. In this case, the total sensing energy consumption during a 24-hour period is equal to 7,721.4 J. Values between these two extreme cases influence the maximum probability of error and the sensing energy consumption in the sensor layer. For a specific value of the RMSE

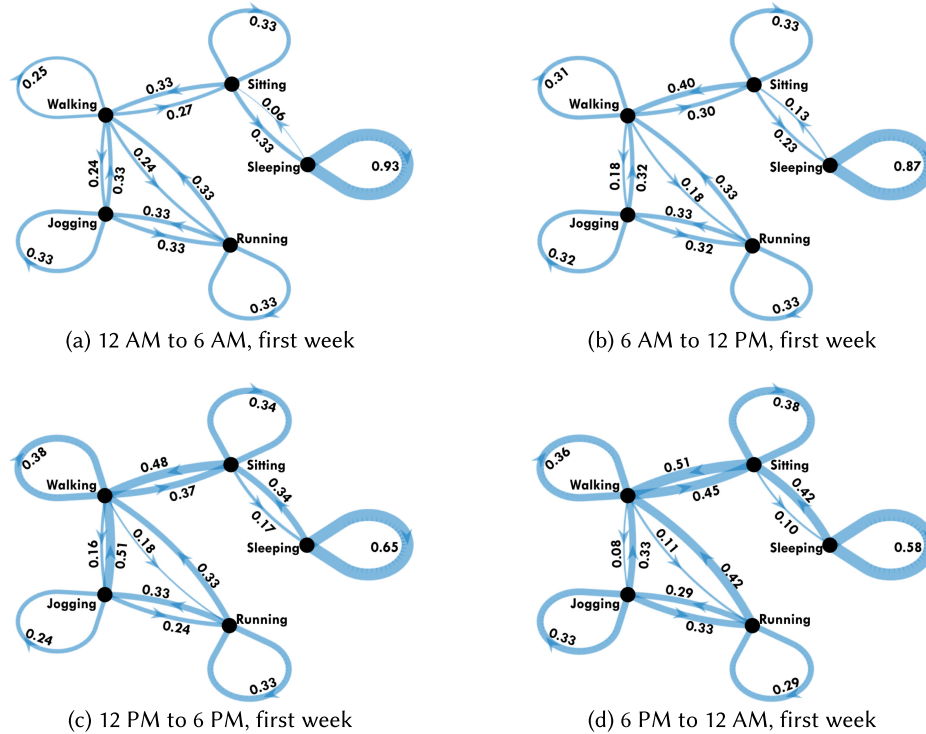


Fig. 12. Markov chain of activities of a subject in a 24-hour period with average transition probabilities calculated from first week in a month.

threshold, increasing the maximum probability of error will let the system monitor the subject less accurately using a lower current level. Therefore, the sensing energy consumption in the sensor will decrease.

MDP strategy. The *myopic* strategy only considers the instantaneous state of the system. Intuitively, a strategy incorporating a longer-term evaluation of the outcome of actions can control the current level to avoid outage, which inevitably reduces performance, saving energy until the subject is more likely to charge. We emphasize that this planning is performed on a nonhomogeneous model, where transition probabilities are a function of the time of the day. This further emphasizes the need for wise planning, aligning energy availability with periods of the day most likely presenting vigorous activities. We further remark that such planning is informed by highly personalized models, capturing the dynamics of the specific person wearing the sensor.

Figure 12 shows the transition probabilities during one day for one of the monitored subjects obtained training the model over 1 week. This specific subject's activities mostly included sleeping between 12 AM and 6 AM, with a probability of 0.937 to remain in the sleeping state and 0.063 of transitioning to the sitting state. The probability of staying in a sleeping state reduces to 0.58 and transitioning to a sitting state increases to 0.42 in the temporal period between 6 PM and 12 AM because of a decrease in the sleeping state. In addition, the Markov chain for each period can be updated after each week. Figure 13 shows the transition probabilities extracted between 12 PM and 6 PM trained over a 1 month period. The individual has a decrease in the probability of staying in the sleeping state from 0.65 to 0.50 over the span of 4 weeks. Meanwhile, the probability of remaining in the sitting state increased from 0.34 to 0.44.

Figure 14 illustrates how the activity of this specific individual evolves over 1 month. For instance, the subject had a decline in walking time from the first week to the third week but then had an increase in her fourth week.

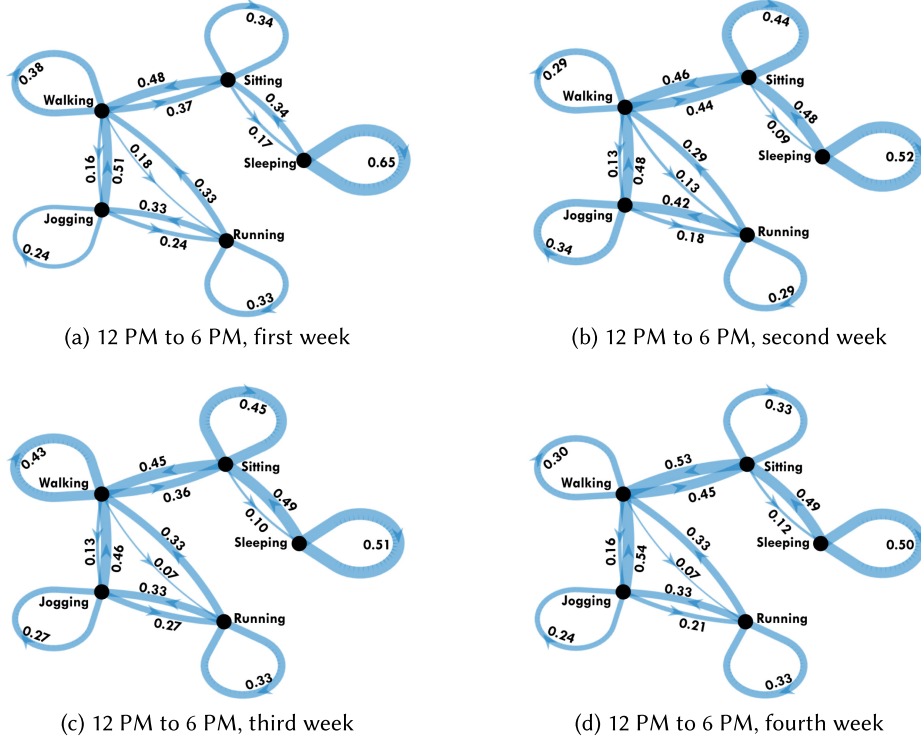


Fig. 13. Markov chain of activities of a subject between 12 PM and 6 PM with average transition probabilities calculated from weekly activities over the span of 4 weeks.

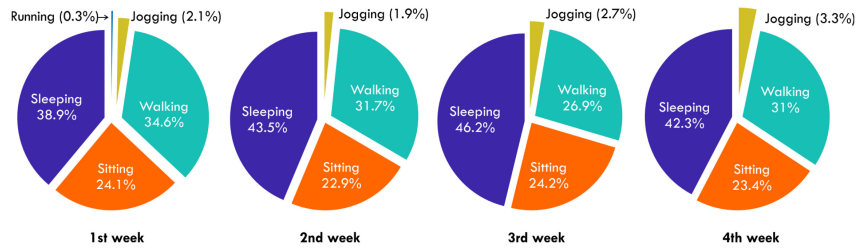


Fig. 14. Weekly activity percentage for 1 month.

In contrast, the sleeping state had an increase of 8% from week 1 to week 3 and dropping by 4% on week 4. Clearly, these changes should be reflected in the control strategy and planning.

Figure 15 compares the *myopic* and MDP strategies for the aforementioned subject over a 48-hour monitoring period. We set the threshold for the probability of error (e.g., ζ in Equation (14)) to 0.002. The MDP cost function, which captures a trade-off between the upper-bound misdetection probability and energy consumption, is a function of the weight $0 \leq \omega \leq 1$. If the value of ω is close to zero, the control strategy tends to privilege lower current levels and higher probability of misdetection. In contrast, a value of ω close to 1 pushes the actions to compromise energy saving to achieve a lower error probability. In this experiment, we set $\omega = 0.176$ to have the closest probability of misdetection to that of the *myopic* strategy in the previous results.

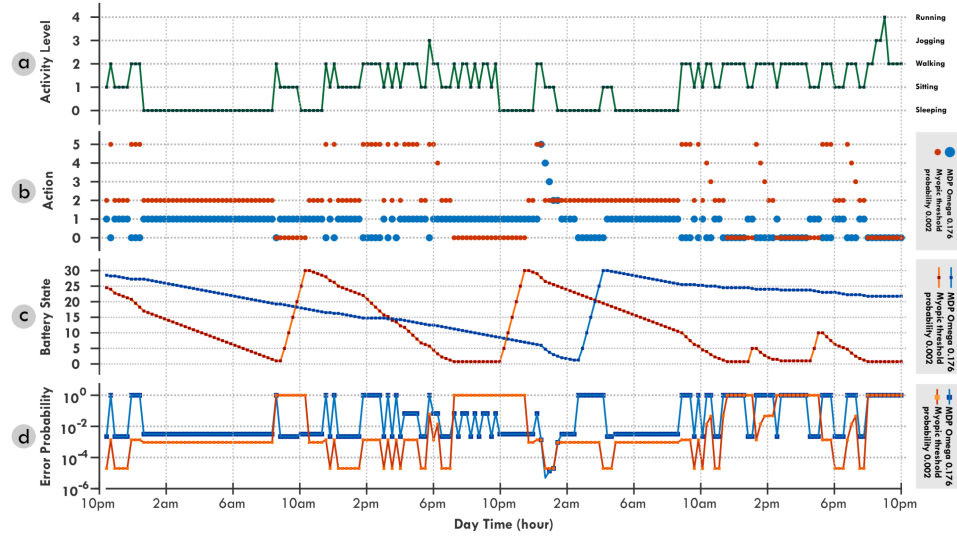


Fig. 15. The 48-hour health monitoring of a healthy person during first week of monitoring. (a) User's activity level. (b) Sensor's sensing power consumption. (c) Battery state tracking based on the sensor's power consumption. (d) Probability of error expected regarding the user's activity. The red line and blue line indicate the *myopic* and MDP methods, respectively.

Figure 15(b) shows the optimal current level selected by the *myopic* and MDP methods. Figure 15(b) and (c) show the actions and dynamics of the battery state induced by the two methods' actions, respectively. The system tracks the battery state for both methods, with 30 being the highest charging state. Based on the optimal action taken, the battery state will be updated at each given time during sensing. During each time, the user charges the battery the sensing stops and the state of battery will be updated.

Figure 15(d) shows the probability of error corresponding to the current level chosen in the optimal current level chosen based on Figure 15(b). At each given time, the system chooses an optimal action based on the user's activity. The *myopic* strategy chooses the optimal action by considering the current activity of an individual. However, the MDP strategy plans based on the current state of the battery and the activity of a user. Therefore, the battery is drained after a longer time in the MDP method compared to *myopic*. The *myopic* method chooses the optimal action without taking into account that the action chosen will drain the battery faster, and this will increase the possibility that the battery will be drained during strenuous activity such as walking, jogging, and running. The battery will not be charged until the user is sleeping or sitting. The *myopic* method chooses a higher current level that will have lower probability of misdetection compared to MDP in a short term. However, the frequency of necessity to charge the battery will be decreased in MDP, resulting in using the resource of the battery more wisely. For instance, between 6 PM and 10 PM of the first 24-hour monitoring, the user was walking, but due to drainage of the battery, the sensor was in sleeping mode. However, the MDP strategy chose the current level U_1 and monitored the user for a longer time.

To update the activity model, the system retrains the MDP model weekly. The MDP model based on activity history from the first week is used to find the optimal solution in Figure 16. Respectively, Figures 17 and 18 show the results of 48 hours of monitoring during the third and fourth week, respectively, of results starting at 10 PM and ending 48 hours later.

Figure 19 shows the probability of error over the entire day as a function of the average energy consumption averaged over a month. We compare the three methods: *myopic*, MDP, and static power allocation.

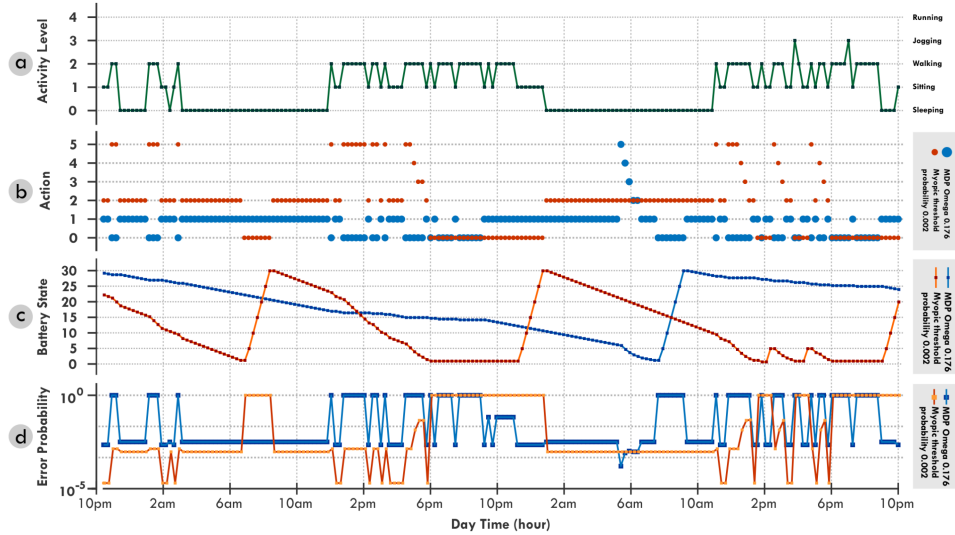


Fig. 16. The 48-hour health monitoring of a healthy person during the second week of monitoring. (a) User's activity level. (b) Sensor's sensing power consumption. (c) Battery state tracking based on the sensor's power consumption. (d) Probability of error expected regarding the user's activity. The red line and blue line indicate the *myopic* and MDP methods, respectively.

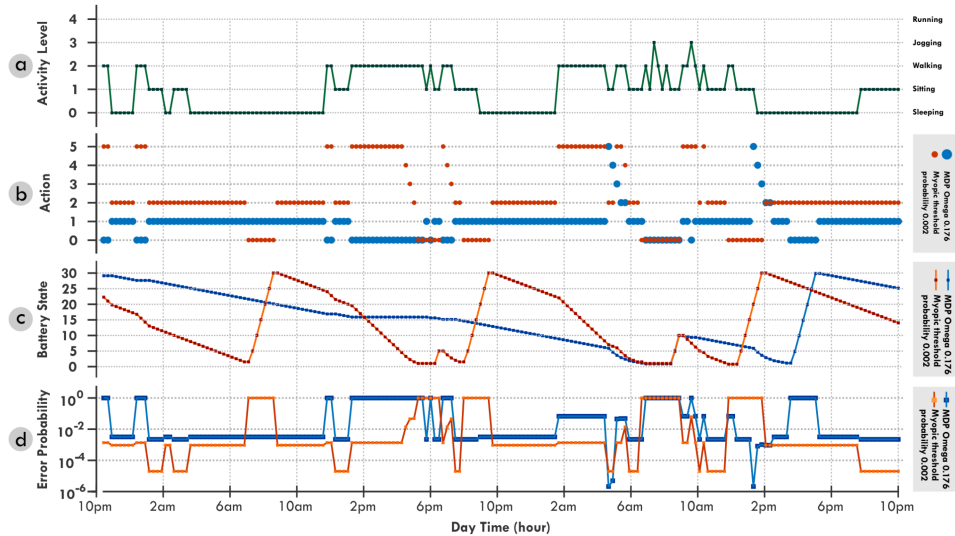


Fig. 17. The 48-hour health monitoring of a healthy person during the third week of monitoring. (a) User's activity level. (b) Sensor's sensing power consumption. (c) Battery state tracking based on the sensor's power consumption. (d) Probability of error expected regarding the user's activity. The red line and blue line indicate the *myopic* and MDP methods, respectively.

Note that the sensor has five current levels—that is, $U \in \{0.8 \text{ mA}, 3.5 \text{ mA}, 6.2 \text{ mA}, 9.2 \text{ mA}, 12 \text{ mA}\}$. We take into account the time slots in which the sensor is off due to battery outage, impacting the average energy consumption and the probability of misdetection in abnormality. Note that the highest current level (e.g., 12 mA) consumes the highest amount of energy but quickly drains the battery, thus inducing an outage approximately

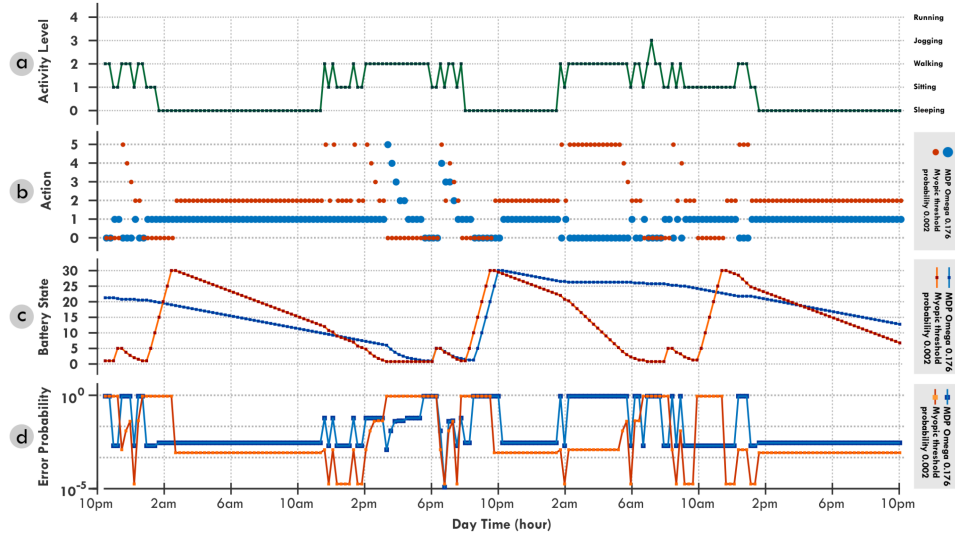


Fig. 18. The 48-hour health monitoring of a healthy person during the fourth week of monitoring. (a) User's activity level. (b) Sensor's sensing power consumption. (c) Battery state tracking based on the sensor's power consumption. (d) Error probability in abnormality detection expected regarding the user's activity. The red line and blue line indicate the *myopic* and MDP methods, respectively.

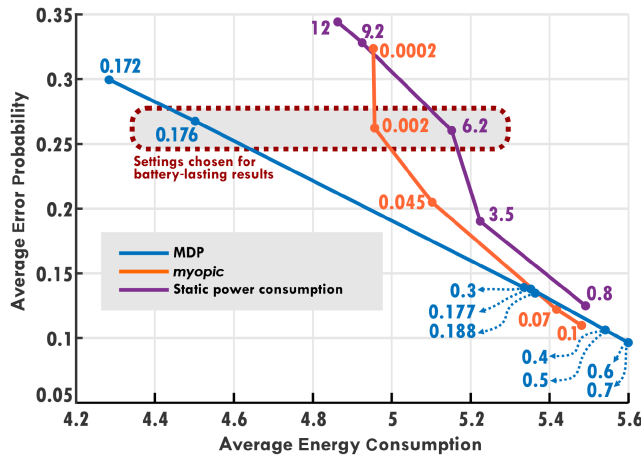


Fig. 19. Average of probability of error as a function of energy consumption (KJ) in 1 month for one subject. Comparison between three methods of MDP, *myopic*, and static power consumption. The *myopic* method is evaluated based on $\zeta \in \{0.0002, 0.002, 0.045, 0.07, 0.1\}$ in Equation (14). MDP is evaluated based on $\omega \in \{0.172, 0.176, 0.177, 0.188, 0.3, 0.4, 0.5, 0.6, 0.7\}$ in Equation (20). Static power consumption is evaluated based on current levels $U \in \{0.8 \text{ mA}, 3.5 \text{ mA}, 6.2 \text{ mA}, 9.2 \text{ mA}, 12 \text{ mA}\}$.

every 6 hours. Note that due to the frequent outages, and thus the frequent 1.5-hour charging periods, the average energy consumption over the 24 hours is smaller than in other current levels. However, during the charging mode, the probability of abnormality misdetection is equal to 1, resulting in a large misdetection probability. Using a constant current level of 0.8 mA increases the average 24-hour energy consumption but leads to a low

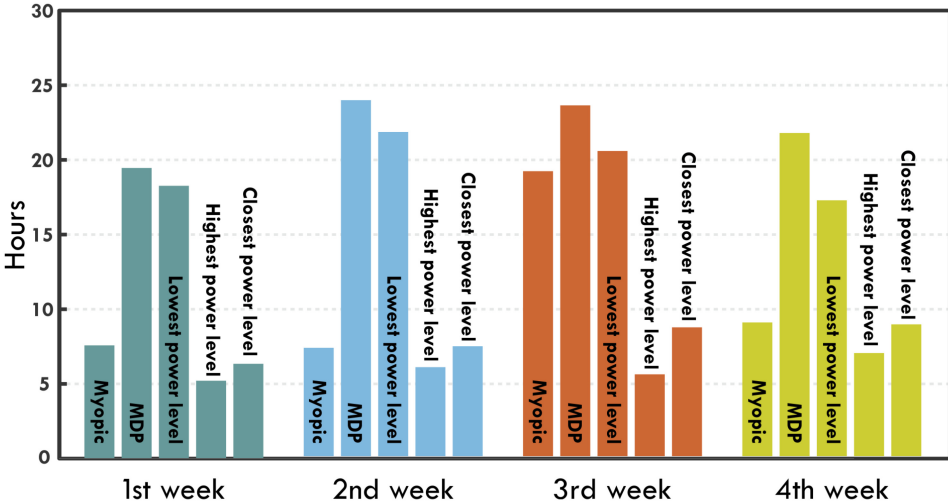


Fig. 20. Average battery lasting over 1 month.

probability of detecting anomalies in difficult states. The dynamic context-aware selection operated by the *myopic* and MDP frameworks is therefore instrumental to achieve good performance.

To derive the MDP-based strategy, we set the parameter of cost function (e.g., ω in Equation (20)) to $\{0.172, 0.176, 0.177, 0.188, 0.3, 0.4, 0.5, 0.6, 0.7\}$ to determine the importance of energy consumption over error probability. Comparing MDP to *myopic* and the constant current level, we see a great reduction in energy consumption when the probability of error is around 0.25. To compare the battery lasting for the three methods, we chose the parameters to satisfy the fixed probability of error 0.26. In this case, the parameter for MDP cost function ($\omega = 0.176$), parameter for upper bound probability of error in the *myopic* method ($\zeta = 0.1$), and static current level is chosen as 6.2 mA.

Using the settings mentioned earlier, we calculated the average time between consecutive battery outages and compared the methods in Figure 20. We also included the battery lasting using the highest and lowest current level in the sensor (e.g., 12 mA and 0.8 mA accordingly).

According to Figure 20, results indicate that MDP even achieves higher efficiency compared to the time we choose the lowest power level. This is because MDP policy chooses the sleeping mode in the sensor when the battery has very low charge, leading to longer periods between battery outages. Results show that MDP doubles the battery duration compared to the *myopic* strategy.

We observe a considerable increase of battery lasting in the third week granted by the *myopic* approach compared to the other weeks for this specific user. The increase is motivated by the evolution of the statistics of the activity pattern, which is illustrated in Figure 14. The user has an increase in the fraction of time spent sleeping and sitting, which grow to 46% and 24%. Therefore, based on our model, this user had a higher probability to charge her wearable device. Consequently, the battery was fully charged more often compared to other weeks. Furthermore, during these activities, the sensor can use a lower power level, resulting in a longer battery duration even when using a simple approach.

Figure 21 shows the comparison between MDP, *myopic*, and static power allocation strategies averaged over 14 subjects. We set a fixed value of average probability of error to 0.32. The MDP strategy consumes 3.7 KJ over 1 month, whereas the *myopic* method consumes 4.42 KJ and the static power allocation strategy consumes 4.4 when using a current level of 9.2 mA. Therefore, MDP has an average of 12% reduction in energy consumption, fulfilling the same probability of error compared to *myopic* and static power consumption.

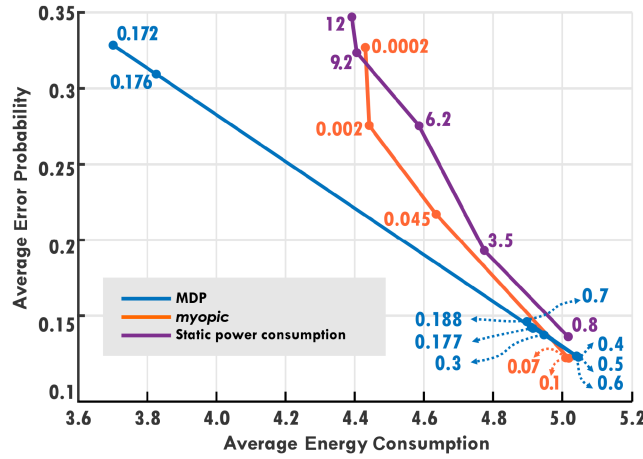


Fig. 21. Average probability of error as a function of energy consumption (KJ) in 1 month averaged over 14 subjects. Comparison between three methods of MDP, *myopic*, and static power consumption. The *myopic* method is evaluated based on $\zeta \in \{0.0002, 0.002, 0.045, 0.07, 0.1\}$ in Equation (14). MDP is evaluated based on $\omega \in \{0.172, 0.176, 0.177, 0.188, 0.3, 0.4, 0.5, 0.6, 0.7\}$ in Equation (20). Static power consumption is evaluated based on current levels $U \in \{0.8 \text{ mA}, 3.5 \text{ mA}, 6.2 \text{ mA}, 9.2 \text{ mA}, 12 \text{ mA}\}$.

7 CONCLUSION

The IoT paradigm, through a high-level network of connected devices, enables ubiquitous health monitoring for patients at risk in everyday settings. Such a remote IoT-based health monitoring system typically includes battery-powered sensors that require a satisfactory energy-efficient control approach. Contemporary published approaches mostly focus on optimizing the power consumption of the sensor layer, which may compromise the accuracy of measurements.

In this article, we proposed two frameworks—*myopic* and MDP—to control the energy-constrained sensor layer. We used the key low-latency characteristics of edge computing to build a context-aware control system whose objective is to adaptively determine the sensing accuracy, and thus the energy dissipation, to maximize the sensor lifetime. We modeled the accuracy of sensor measurement in capturing abnormality as a Gaussian distribution. The optimization problem minimizes the energy consumption within different contexts (e.g., activity) to achieve a satisfactory probability of misdetection in abnormality. We extend our implementations to monitor 14 healthy subjects for 1 month.

We demonstrated that the *myopic* method has savings of 16.9% on average compared to the nonadaptive case in a 24-hour health monitoring period by adapting to an activity while assuring a minimum level of probability of misdetection in abnormality. Moreover, our results show that MDP can increase the battery lasting with an average of more than two times compared to *myopic* and nonadaptive power consumption, fulfilling the same probability of misdetection over 1 month. As future work, we will investigate calculating the distance of adjacent policies among different subjects.

REFERENCES

- [1] Farshad Firouzi, Amir M. Rahmani, Kunal Mankodiya, Mustafa Badaroglu, Geoff V. Merrett, P. Wong, and Bahar Farahani. 2018. Internet-of-Things and big data for smarter healthcare: From device to architecture, applications and analytics. *Future Generation Computer Systems* 78, Pt. 2 (2018), 583–586.
- [2] Riitta Mieronskoski, Iman Azimi, Amir M. Rahmani, Riku Aantaa, Virpi Terävä, Pasi Liljeberg, and Sanna Salanterä. 2017. The Internet of Things for basic nursing –A scoping review. *International Journal of Nursing Studies* 69 (2017), 78–90.

- [3] S. M. Riazul Islam, Daehan Kwak, M. D. Humaun Kabir, Mahmud Hossain, and Kyung-Sup Kwak. 2015. The Internet of Things for health care: A comprehensive survey. *IEEE Access* 3 (2015), 678–708.
- [4] A. M. Rahmani, P. Liljeberg, J.-S. Preten, and A. Jantsch (Eds.). 2017. *Fog Computing in the Internet of Things: Intelligence at the Edge*. Springer.
- [5] Delaram Amiri, Arman Anzaniour, Iman Azimi, Amir M. Rahmani, Pasi Liljeberg, Nikil Dutt, and Marco Levorato. 2019. Optimizing energy in wearable devices using fog computing. In *Fog Computing: Theory and Practice*. Wiley. arXiv:1907.11989.
- [6] Amir M. Rahmani, Tuan Nguyen Gia, Behailu Negash, Arman Anzaniour, Iman Azimi, Mingze Jiang, and Pasi Liljeberg. 2018. Exploiting smart e-Health gateways at the edge of healthcare Internet-of-Things: A fog computing approach. *Future Generation Computer Systems* 78 (2018), 641–658.
- [7] Sina Shahhosseini, Iman Azimi, Arman Anzaniour, Axel Jantsch, Pasi Liljeberg, Nikil Dutt, and Amir M. Rahmani. 2019. Dynamic computation migration at the edge: Is there an optimal choice? In *Proceedings of the 2019 Great Lakes Symposium on VLSI (GLSVLSI '19)*. ACM, New York, NY, 519–524.
- [8] Toshiyo Tamura, Yuka Maeda, Masaki Sekine, and Masaki Yoshida. 2014. Wearable photoplethysmographic sensors—Past and present. *Electronics* 3, 2 (2014), 282–302.
- [9] Delaram Amiri, Arman Anzaniour, Iman Azimi, Marco Levorato, Amir M. Rahmani, Pasi Liljeberg, and Nikil Dutt. 2018. Edge-assisted sensor control in healthcare IoT. In *Proceedings of the 2018 IEEE Global Communications Conference (GLOBECOM'18)*. IEEE, Los Alamitos, CA, 1–6.
- [10] Emad Kasaian Naeini, Iman Azimi, Amir M. Rahmani, Pasi Liljeberg, and Nikil Dutt. 2019. A real-time PPG quality assessment approach for healthcare Internet-of-Things. *Procedia Computer Science* 151 (2019), 551–558.
- [11] Kun Wang, Yihui Wang, Yanfei Sun, Song Guo, and Jinsong Wu. 2016. Green industrial Internet of Things architecture: An energy-efficient perspective. *IEEE Communications Magazine* 54, 12 (2016), 48–54.
- [12] Chunsheng Zhu, Victor C. M. Leung, Laurence T. Yang, and Lei Shu. 2015. Collaborative location-based sleep scheduling for wireless sensor networks integrated with mobile cloud computing. *IEEE Transactions on Computers* 64, 7 (2015), 1844–1856.
- [13] Dayong Ye and Minjie Zhang. 2018. A self-adaptive sleep/wake-up scheduling approach for wireless sensor networks. *IEEE Transactions on Cybernetics* 48, 3 (2018), 979–992.
- [14] Yanwen Wang, Hainan Chen, Xiaoling Wu, and Lei Shu. 2016. An energy-efficient SDN based sleep scheduling algorithm for WSNs. *Journal of Network and Computer Applications* 59 (2016), 39–45.
- [15] Jae-Han Jeon, Hee-Jung Byun, and Jong-Tae Lim. 2013. Joint contention and sleep control for lifetime maximization in wireless sensor networks. *IEEE Communications Letters* 17, 2 (2013), 269–272.
- [16] Sarder Fakhru1 Abedin, Md Golam Rabiul Alam, Rim Haw, and Choong Seon Hong. 2015. A system model for energy efficient green-IoT network. In *Proceedings of the 2015 International Conference on Information Networking (ICOIN'15)*. IEEE, Los Alamitos, CA, 177–182.
- [17] Ovidiu Vermesan, Peter Friess, Patrick Guillemin, Sergio Gusmeroli, Harald Sundmaeker, Alessandro Bassi, Ignacio Soler Jubert, et al. 2011. Internet of Things strategic research roadmap. *Internet of Things—Global Technological and Societal Trends* 1, 2011 (2011), 9–52.
- [18] Navroop Kaur and Sandeep K. Sood. 2017. An energy-efficient architecture for the Internet of Things (IoT). *IEEE Systems Journal* 11, 2 (2017), 796–805.
- [19] Caglar Tunc and Nail Akar. 2017. Markov fluid queue model of an energy harvesting IoT device with adaptive sensing. *Performance Evaluation* 111 (2017), 1–16.
- [20] Lin-Huang Chang, Tsung-Han Lee, Shu-Jan Chen, and Cheng-Yen Liao. 2013. Energy-efficient oriented routing algorithm in wireless sensor networks. In *Proceedings of the 2013 IEEE International Conference on Systems, Man, and Cybernetics (SMC'13)*. IEEE, Los Alamitos, CA, 3813–3818.
- [21] Gitanjali Pradhan, Rajni Gupta, and Suparna Biswasz. 2018. Study and simulation of WBAN MAC protocols for emergency data traffic in healthcare. In *Proceedings of the 2018 5th International Conference on Emerging Applications of Information Technology (EAIT'18)*. IEEE, Los Alamitos, CA, 1–4.
- [22] Daphney-Stavroula Zois, Marco Levorato, and Urbashi Mitra. 2012. A POMDP framework for heterogeneous sensor selection in wireless body area networks. In *Proceedings of IEEE INFOCOM 2012*. IEEE, Los Alamitos, CA, 2611–2615.
- [23] D.-S. Zois, M. Levorato, and U. Mitra. 2014. Active classification for POMDPs: A Kalman-like state estimator. *IEEE Transactions on Signal Processing* 62, 23 (2014), 6209–6224.
- [24] Daphney-Stavroula Zois, Marco Levorato, and Urbashi Mitra. 2013. Energy-efficient, heterogeneous sensor selection for physical activity detection in wireless body area networks. *IEEE Transactions on Signal Processing* 61, 7 (2013), 1581–1594.
- [25] Peter H. Charlton, Timothy Bonnici, Lionel Tarassenko, David A. Clifton, Richard Beale, and Peter J. Watkinson. 2016. An assessment of algorithms to estimate respiratory rate from the electrocardiogram and photoplethysmogram. *Physiological Measurement* 37, 4 (2016), 610.
- [26] Marco A. F. Pimentel, Peter H. Charlton, and David A. Clifton. 2015. *Probabilistic estimation of respiratory rate from wearable sensors*. In *Wearable Electronics Sensors*. Springer, 241–262.
- [27] Walter Karlen, Srinivas Raman, J. Mark Ansermino, and Guy A. Dumont. 2013. Multiparameter respiratory rate estimation from the photoplethysmogram. *IEEE Transactions on Biomedical Engineering* 60, 7 (2013), 1946–1953.

- [28] Ainara Garde, Walter Karlen, J. Mark Ansermino, and Guy A. Dumont. 2014. Estimating respiratory and heart rates from the correntropy spectral density of the photoplethysmogram. *PLoS One* 9, 1 (2014), e86427.
- [29] L.-G. Lindberg, H. Ugnell, and P. Å. Öberg. 1992. Monitoring of respiratory and heart rates using a fibre-optic sensor. *Medical and Biological Engineering and Computing* 30, 5 (1992), 533–537.
- [30] Maxim Integrated. 2018. *High-Sensitivity Pulse Oximeter and Heart-Rate Sensor for Wearable Health*. Retrieved November 1, 2018 from <https://www.maximintegrated.com/en/products/sensors/MAX30102.html>.
- [31] Garmin. 2018. Vivosmart HR | Activity Tracker. Retrieved November 1, 2018 from <https://buy.garmin.com/en-US/US/p/531166>.
- [32] C. Tudor-Locke, S. B. Sisson, T. Collova, S. M. Lee, and P. Swan. 2005. Pedometer-determined step count guidelines for classifying walking intensity in a young ostensibly healthy population. *Canadian Journal of Applied Physiology* 30, 6 (2005), 666–76.
- [33] Catrine Tudor-Locke, Sarah M. Camhi, Claudia Leonardi, William D. Johnson, Peter T. Katzmarzyk, Conrad P. Earnest, and Timothy S. Church. 2011. Patterns of adult stepping cadence in the 2005–2006 NHANES. *Preventive Medicine* 53, 3 (2011), 178–181.

Received February 2019; revised May 2019; accepted July 2019